

HybridMIM: A Hybrid Masked Image Modeling Framework for 3D Medical Image Segmentation

Zhaohu Xing, Lei Zhu, *Member, IEEE*, Lequan Yu, *Member, IEEE*, Zhiheng Xing, and Liang Wan, *Member, IEEE*

Abstract—Masked image modeling (MIM) with transformer backbones has recently been exploited as a powerful self-supervised pre-training technique. The existing MIM methods adopt the strategy to mask random patches of the image and reconstruct the missing pixels, which only considers semantic information at a lower level, and causes a long pre-training time. This paper presents HybridMIM, a novel hybrid self-supervised learning method based on masked image modeling for 3D medical image segmentation. Specifically, we design a two-level masking hierarchy to specify which and how patches in sub-volumes are masked, effectively providing the constraints of higher level semantic information. Then we learn the semantic information of medical images at three levels, including: 1) partial region prediction to reconstruct key contents of the 3D image, which largely reduces the pre-training time burden (pixel-level); 2) patch-masking perception to learn the spatial relationship between the patches in each sub-volume (region-level), and 3) drop-out-based contrastive learning between samples within a mini-batch, which further improves the generalization ability of the framework (sample-level). The proposed framework is versatile to support both CNN and transformer as encoder backbones, and also enables to pre-train decoders for image segmentation. We conduct comprehensive experiments on four widely-used public medical image segmentation datasets, including BraTS2020, BTCV, MSD Liver, and MSD Spleen. The experimental results show the clear superiority of HybridMIM against competing supervised methods, masked pre-training approaches, and other self-supervised methods, in terms of quantitative metrics, timing performance and qualitative observations. The codes of HybridMIM are available at <https://github.com/ge-xing/HybridMIM>.

Index Terms—Self-supervised learning, masked image modeling, 3D medical image segmentation.

I. INTRODUCTION

This paragraph of the first footnote will contain the date on which you submitted your paper for review. This work was supported in part by Tianjin Natural Science Foundation under Grant 21JCYBJC00510 and HKU Seed Fund for Basic Research (Project No. 202111159073).

Zhaohu Xing is with Medical College of Tianjin University, P. R. China (e-mail: xingzhaohu@tju.edu.cn).

Lei Zhu is with The Hong Kong University of Science and Technology, Hong Kong, and The Hong Kong University of Science and Technology (Guangzhou), China (e-mail: leizhu@ust.hk).

Lequan Yu is with The University of Hong Kong, Hong Kong (e-mail: lqyu@hku.hk).

Zhiheng Xing is with Haihe Hospital, Tianjin University, China (e-mail: 18920696025@189.cn).

Liang Wan is with Medical College, and the College of Computing and Intelligence, Tianjin University, China (e-mail: lwan@tju.edu.cn)

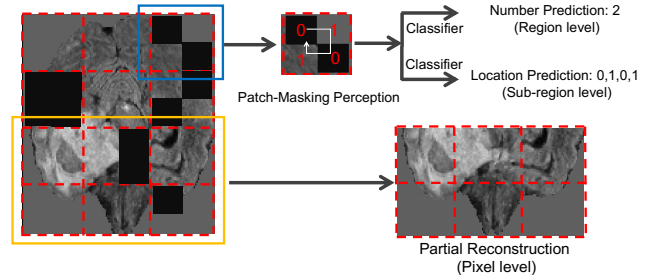


Fig. 1: Illustration of our key idea in the 2D form. We regularly divide the input image into two-levels of patches, masking sub-regions or patches randomly. The masking information is encoded into binary, providing the locations and number of masked patches. In addition, local regions are selected for reconstruction, which facilitates a faster pre-training efficiency for high-dimensional medical images.

IN the field of medical image analysis [1]–[3], automatic medical image segmentation remains a hot topic to facilitate lesion diagnosis and quantification, as well as treatment planning and evaluation. In recent decades, many deep learning-based algorithms for medical image segmentation have been developed to obtain improved segmentation performance. It is worth noting that training deep learning-based algorithms usually requires a large amount of manually labeled data. Yet in the field of medical image analysis, the amount of labeled 3D medical data is often small compared to natural images, since labeling 3D medical data is not only tedious and time-consuming, but also needs intensive involvement of physicians to provide considerable domain expertise [4].

To alleviate the problem of insufficient labeled data, self-supervised learning (SSL) schemes [5]–[8] have been developed to learn a generic representation of unlabeled data, and the obtained models can have faster convergence and higher accuracy when fine-tuned for downstream tasks. Typical self-supervised learning schemes include using tailored proxy tasks [9], [10], self-supervised contrastive learning [11], and masked image modeling [12]. The former designs specific pretext tasks, such as inpainting, random rotation, distortion, for image restoration. Contrastive learning learns the relational characteristics between different samples by constructing positive and negative sample pairs. Masked image modeling, which is a recently developed technique, exhibits good potentials by learning the hidden context features through predicting what the masked parts of the input data should be.

It is noted that most self-supervised learning methods are developed for natural images, and may not migrate well to

the medical image domain [13], since 3D medical image data has much higher dimensionality and can contain multiple modalities. There have been several approaches to explore how to apply self-supervised learning to 3D medical images. For example, the visual word learning [14] uses auto-encoder to actively discover semantic visual words and takes them as self-supervised learning labels, allowing the model to learn the rich semantic information. However, its pre-training requires the construction of self-supervised learning labels, resulting in more pre-training burden. UNetFormer [15] utilizes a 3D Swin Transformer encoder, and directly applies masked image modeling by predicting randomly masked volumetric tokens. Just like current MAE [12] and SimMIM methods [16], it recovers missing pixels, which are from a lower semantic level. What's more, reconstructing the whole image is time-consuming and leads to slow pre-training performance.

In this paper, we propose a new hybrid self-supervised learning framework (HybridMIM) based on hierarchical masked image modeling for 3D medical image segmentation. Our framework learns the comprehensive semantic representation of 3D unlabeled medical images at pixel/region/sample three levels. Specifically, as illustrated in Figure 1, we design a two-level masking hierarchy to support masking sub-regions or patches randomly, and propose a joint self-supervised learning to account for semantic information at different levels. At the pixel level, instead of predicting all the masked patches as MAE [12], we utilize a partial region prediction scheme to reconstruct key parts of the 3D images, which can largely accelerate the pre-training. The masking status which reflects the locations and number of masked sub-regions, can help the model to characterize anatomical information at region-level. Finally, we utilize a dropout-based contrastive learning strategy at the sample level, to improve the model's capability of discrimination between different samples.

Our proposed HybridMIM is compatible with different network architectures, and we adopt UNet and SwinUNETR as the underlying architectures. The effectiveness of our method is validated via two evaluation modes: pre-training and finetuning using the same data or using different data, on four downstream segmentation tasks, including BraTS2020 [17], [18], BTCV [19], MSD-Spleen and MSD-Liver [20], which cover different organs, different object numbers and multi-modalities. The comprehensive experimental results show that our HybridMIM outperforms existing state-of-the-art self-supervised methods in terms of both downstream segmentation task accuracy and training efficiency.

In summary, our HybridMIM self-supervised learning method has the following dominant features:

- **Compatibility.** Our method can serve as a general pre-training framework, and we demonstrate that it supports both multi-scale convolutional neural network and transformer network architectures.
- **Comprehensiveness.** Our method is designed to learn the semantic information within the data from pixel-level, region-level to sample-level.
- **Robustness.** Our method is proved to outperform SOTA methods in accuracy and training efficiency for multiple widely-used public segmentation datasets.

II. RELATED WORK

A. SSL via Tailored Proxy Tasks

This category of methods usually constructs self-supervised learning labels by designing pretext tasks. There are several commonly used pretext tasks in natural image processing. Image inpainting is adopted to learn visual representations by predicting the original image region [21]. Jigsaw puzzles solving [22] learns structural information about images by randomly disrupting image patches and restoring them. In addition, random rotation estimation [9] enhances the understanding of images by randomly rotating images and using the network to predict the rotation angles.

One typical work using tailored proxy tasks in the medical imaging is Models Genesis [10]. It uses a variety of ways, such as distortion or painting-based methods, to disrupt pixels in the original image [9], [21], [23], and then utilize a network of encoder-decoder structure for restoration. This method mainly focuses on the prediction of local information. TransVW [14] classifies different image regions as semantic visual words, and reconstructs randomly masked visual word regions while predicting the region's category. The method achieves improved performance on downstream tasks, while it needs to find semantic visual words first, thus leading to more pre-training burden. Yucheng Tang *et al.* [13] pre-trained swin transformers via three proxy tasks: inpainting, rotation and contrastive learning. Our method is built on the masked image modeling strategy, and constructs three proxy tasks at different levels, including predicting the partial masked region at pixel level, estimating the masking distribution at region level, and dropout-based contrastive learning at sample level.

B. SSL via Contrastive Learning

Contrastive learning is also a common approach in self-supervised learning, which centers on learning the relational features between samples by using different ways to construct positive and negative sample pairs. A common way to construct sample pairs is data augmentation, in which one sample is augmented to form positive sample pairs, and different samples within a mini-batch are taken as negative sample pairs. In medical imaging, Yucheng Tang *et al.* [13] used contrast learning based on such data augmentation as one of the tailored proxy tasks, and had verified its effectiveness through numerous experiments.

Additionally, in the NLP filed, the SimCSE method [11] proposes to use dropout to construct positive and negative samples. The method adds a dropout layer in the network and feed forward an input sample twice to obtain two sets of features. Features from the same sample are taken as positive samples, while features from different samples form negative samples. This scheme is easy to implement, and achieves good performance. We utilize SimCSE scheme to construct our contrastive learning task.

C. SSL via Masked Image Modeling

More recently, a growing body of works is exploring to apply the idea of masked language modeling, which is successful

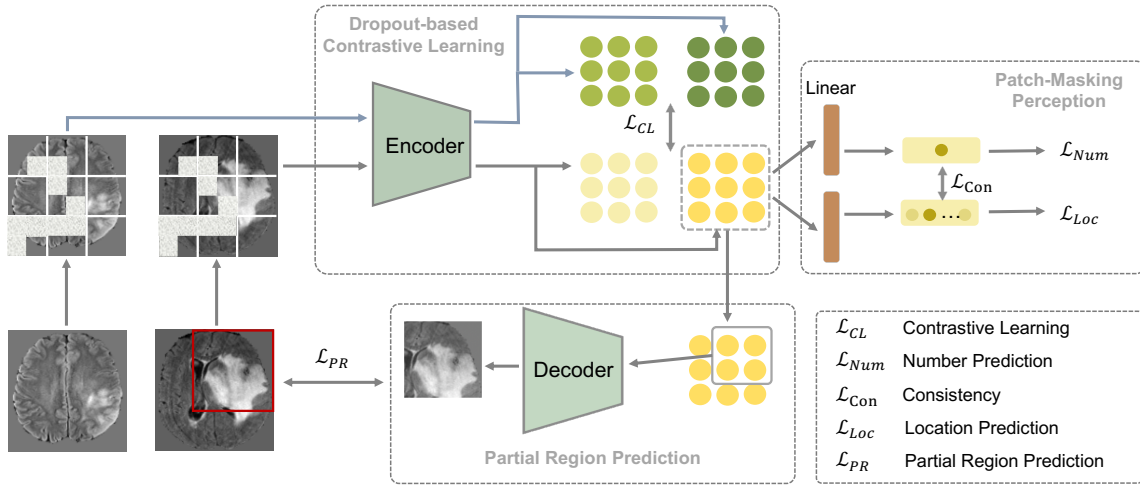


Fig. 2: Overview of the HybridMIM pre-training framework. Input 3D medical images (demonstrated in 2D form) are randomly masked with a two-level masking strategy, then fed to the encoder twice to obtain two sets of feature representations. We use patch-masking perception, partial region reconstructions, and dropout-based contrastive learning as proxy tasks to learn contextual representations of input images.

in the NLP field, to natural imaging. Masked Autoencoders (MAE) [12], built on ViT architecture, masks random image patches and reconstructs the missing pixels by an asymmetric transformer autoencoder. To accelerate the pretraining speed, MAE discard masked tokens, which makes it less compatible with multi-scale processing expected in medical imaging. Meanwhile, the SimMIM [16] achieves masked image modeling by utilizing multi-scale encoders such as Swin transformer and ResNet. SimMIM preserves the masked image tokens in the computation, and utilizes one convolutional layer as the decoder to increase timing performance, which may not handle well high-dimensional and high-resolution medical images.

UNetFormer [15] directly applies the idea of masked image modeling in medical imaging. It uses a 3D SwinTransformer structure as the encoder and a multi-scale CNN or SwinTransformer structure as the decoder, to reconstruct the randomly masked sub-volumes. However, its structure is fixed and requires an enormous amount of memory during the training process. Our work extends the idea of masked image modeling to consider higher-level constraint on the semantic anatomical information. What's more, we accelerate the pre-training speed by using partial region prediction.

III. HYBRID MASKED IMAGE MODELING

The objective of model pre-training is to effectively encode anatomical information of the human body in unlabeled image data. In this work, we propose a two-level masking strategy to facilitate the exploitation of semantic context within one image, from both pixel and regional views. To further improve the model's ability to discriminate between different samples, we apply dropout-based contrastive learning within a mini-batch. Our pre-training is then accomplished with three proxy tasks, which learns the comprehensive semantic representation of images from pixel-level, region-level, and sample-level views. Figure 2 illustrates the idea, introduced next.

A. Masking Strategy and Network Architectures

Assuming the input 3D medical image is $\mathcal{X} \in \mathcal{R}^{H \times W \times D}$, we first divide it equally into multiple non-overlapping sub-volumes (the first level), and then split each sub-volume along

three dimensions equally, forming 8 smaller patches (the second level). Let R denote the number of first-level sub-volumes, and we will have $8R$ second-level patches in total. Given the division, our masking strategy randomly selects second-level patches to do the masking (removing). Then, for each first-level sub-volume, we know how many and which second-level patches are masked. It is noted that the number and location information of the masked second-level patches can give a higher-level constraint on the anatomical information. Hence, in addition to reconstruct the missing pixels, our HybridMIM also pays attention to the masking distribution so as to better learn the spatial anatomical information.

Following the auto-encoder architecture, our approach has an encoder that maps the input image data to the latent feature representation, and a decoder that reconstructs the original image from latent features. Since 3D medical images are multi-dimensional and have higher resolutions than natural images, we adopt two widely-used multi-scale segmentation models as the underlying infrastructure, including UNet [24] and SwinUNETR [25]. For UNet that is a convolutional neural network, the masked image is feed into as a whole, while for SwinUNETR that is a transformer method, the masked image is split into tokens whose dimension is set the same as that of the second-level patches.

B. Partial Region Prediction

Previous masked image modeling methods [12], [16] learn the feature representation of the image by reconstructing all the pixels values in the masked regions through a decoder. SimMIM [16] accelerates the learning by adopting a linear layer as the decoder. But considering that medical images are multi-dimensional and high-resolution, a multi-scale decoder is needed to reconstruct the image. To speed-up the pre-training process, we only select the features of some first-level sub-volumes (the target region) for reconstruction. The partial reconstruction loss is defined as the L_2 distance between the reconstructed region and masked pixels in the target region,

$$\mathcal{L}_{PR} = \frac{1}{|\hat{R}|} \sum_{r \in \hat{R}} \|c_r - \hat{c}_r\|_2, \quad (1)$$

where \hat{R} is a subset of sub-volumes in the target region, $|\hat{R}|$ is the number of involved sub-volumes, c_r and \hat{c}_r represent the prediction values and the input values, respectively. Since the medical images usually have organs in the middle and may contain empty regions near the image boundary, we manually set the target region for one dataset around the image center.

C. Patch-Masking Perception

Patch-Masking perception predicts the number and locations of masked patches for each sub-volume. This is achieved by adding two separate linear projection layers to the latent feature representation; see Figure 2. As the masked patch number ranges within $[0, 1, \dots, 8]$, we use a 9-dimensional softmax probability vector to represent the predicted number for r -th sub-volume, denoted as u_r . Given the ground truth \hat{u} , a cross-entropy loss is used for number prediction task:

$$\mathcal{L}_{\text{Num}} = -\frac{1}{R} \sum_{r=1}^R \hat{u}_r \log(u_r), \quad (2)$$

where R denotes the number of first-level sub-volume, \hat{u}_r is represented as a one-hot vector.

The predicted location p_r is an 8-dimensional probability vector, with each element representing whether the corresponding patch is masked. Here, we can employ the ℓ_0 loss function [26] for location prediction task, which counts non-zero elements in p_r , defined as:

$$\mathcal{L}_{\text{Loc}} = \sum_{r=1}^R \sum_{k=1}^8 s_r^k, \quad \text{with } s_r^k = \begin{cases} 1 & \text{if } p_r^k \neq 0 \\ 0 & \text{otherwise} \end{cases}, \quad (3)$$

where p_r^k denotes the predicted probability of the k -th patch in the r -th sub-volume, and if $p_r^k=0$, this patch is predicted as a masked patch, otherwise it is a non-masked patch. Since ℓ_0 loss is difficult to optimize, a binary cross-entropy loss function is utilized as an alternative:

$$\mathcal{L}_{\text{Loc}} = -\frac{1}{R} \sum_{r=1}^R \sum_{k=1}^8 \hat{p}_r^k \log p_r^k + (1 - \hat{p}_r^k) \log(1 - p_r^k), \quad (4)$$

where \hat{p} denotes the ground truth for the location coding of masked patches.

In addition, there is a straight-forward constraint between the predicted number and the predicted location information, in which the former can be calculated from the later. Therefore, we define a consistency loss to bridge them:

$$\mathcal{L}_{\text{Con}} = \frac{1}{2} \left(\sum_{r=1}^R CE(u_r, \sum_{k=1}^K \hat{p}_r^k) + MSE(\sum_{k=1}^K p_r^k, \tilde{u}_r) \right), \quad (5)$$

where CE and MSE represent the cross entropy loss and mean squared error, $\hat{p}_r^k = \mathbb{1}[p_r^k > 0.5]$ gives an 0/1 estimate, and $\tilde{u}_r = \text{argmax}(u_r)$ gives the number estimate.

D. Dropout-based Contrastive Learning

In order to further improve the model's generalization ability, we adopt dropout-based contrastive learning that is proven to be effective in the field of natural language processing [11]. Specifically, an masked image is encoded twice and two latent

feature representations will be obtained due to the effect of dropout. Since they come from the same input, they are used as positive samples. The latent feature representations obtained from different images within a mini-batch are taken as negative samples for contrastive learning:

$$\mathcal{L}_{\text{CL}} = -\log \frac{\exp(\text{sim}(v_i, v_j)/t)}{\sum_k^{2N} \mathbb{1}_{k \neq i, j} \exp(\text{sim}(v_i, v_k)/t)}, \quad (6)$$

where t is the measurement of normalized temperature scale. $\mathbb{1}$ is the indicator function evaluating to 1 iff $k \neq i$. v denotes the feature representation extracted by the encoder. $\text{sim}(v_i, v_j)$ denotes the similarity between the representations of positive samples, and $\text{sim}(v_i, v_k)$ denotes the similarity between the representations of negative samples.

E. Loss Function

Formally, we minimize a multi-objective loss functions combining masked region perception, partial reconstruction, and dropout-based contrastive learning losses, as follows:

$$\mathcal{L} = \mathcal{L}_{\text{PR}} + \lambda_1 \mathcal{L}_{\text{Num}} + \lambda_2 \mathcal{L}_{\text{Loc}} + \lambda_3 \mathcal{L}_{\text{Con}} + \lambda_4 \mathcal{L}_{\text{CL}}, \quad (7)$$

where $\lambda_1, \lambda_2, \lambda_3, \lambda_4$ are empirically set as 0.1, 0.1, 0.01, 0.1 respectively in all the experiments.

IV. EXPERIMENTS

A. Datasets

Pre-training Dataset: We collected a total of 1897 CT images to construct our pre-training dataset. They come from 4 public CT image datasets, including the ATM22 [27] (150 cases of chest), luna16 [28] (888 cases of lung), covid-19 [29] (448 cases of lung) and FLARE21 [30] (411 cases of abdomen) datasets.

BraTS2020 dataset: BraTS2020 dataset [17], [18] contains a total of 369 brain MRI images, and each case image has 4 modalities (namely T1, T1Gd, T2, T2-FLAIR) and 3 segmentation targets (WT: whole tumor, ET: enhancing tumor, TC: tumor core). All the data have been resampled to the same spacing (1.0, 1.0, 1.0). Due to the large size of the input image, we crop the training sub-volume of a size of (128,128,128).

BTCV dataset: BTCV [19] contains a total of 30 cases of 3D abdominal multi-organ CT images, with 1 modality and 13 organ segmentation targets per case. All cases are resampled to the same spacing (1.5, 1.5, 2.0). We crop the training sub-volumes of a size of (96,96,96).

We further use two task datasets from MSD dataset [20]. **MSD Liver** contains a total of 201 cases of 3D liver CT images, with 1 modality and 2 segmentation targets (liver, liver tumor) per case. The **MSD Spleen** contains 61 cases of 3D spleen CT images with 1 modality and 1 segmentation target (spleen) per case. For these two datasets, we resample all the cases to the same spacing (1.5, 1.5, 2.0) and crop the training sub-volumes of a size of (96,96,96).

B. Evaluation Modes:

To make a comprehensive comparison, we adopt two evaluation modes to do pre-training and finetuning:

- **Generic pre-training mode:** A generic model is pre-trained on our collected pre-training dataset, and finetuned on the four segmentation tasks.
- **Task-specific pre-training mode:** A task-specific model is pre-trained and finetuned on each segmentation task dataset. To avoid data leakage, we do self-supervised pre-training on the training set of the downstream task datasets, which are all split 80% for training.

In finetuning stage for segmentation, we utilize the pre-trained encoder and decoder by replacing the last layer with a new random $c \times 1 \times 1 \times 1$ convolution layer, where c is the number of segmentation targets.

C. Implementation Details

The default options for the components of HybridMIM are: the two-level masking strategy with a mask ratio of 0.4, the first-level sub-volume size of $32 \times 32 \times 32$, the second-level patch size of $16 \times 16 \times 16$; the partial region prediction with the reconstructed region size of $96 \times 96 \times 96$ for BraTS2020, and $64 \times 64 \times 64$ for BTCV, MSD Liver and MSD Spleen. These settings are determined via multiple control experiment; See Figure 6 for details. For the pre-training dataset, BTCV, MSD liver and MSD spleen, we use randomly cropped images with a resolution of $96 \times 96 \times 96$ and a batch size of 4 per GPU. For BraTS2020 dataset, we use $128 \times 128 \times 128$ as the random crop size and a batch size of 2 per GPU. As each image case in BraTS2020 contains 4 modalities, we concatenate each modality in channel dimension at the input of the network.

Our model is implemented in Pytorch 1.12.1-cuda11.3 and Monai 1.0.0. In both pre-training and finetuning, we use an AdamW [31] optimizer along with a *cosine* learning rate scheduler (an initial learning rate of $1e-4$, a decay of $1e-5$, and a warmup [32] of 50 epochs). We run a total of 10w step for all pre-training experiments, and in finetuning, we run 300 epochs for the BraTS2020 dataset, 2000 epochs for the BTCV dataset, and 600 epochs for the MSD Liver and Spleen datasets. No data augmentation is applied at the pre-training stage, while a light strategy is used in the finetuning: random flip, rotation, intensity scaling and shifts with probabilities of 0.2, 0.2, 0.1, and 0.1, respectively. All experiments are conducted on a cloud computing platform with four NVIDIA A100 Tensor Core GPUs and two NVIDIA Tesla V100 GPUs.

D. Benchmarking

For a thorough evaluation, HybridMIM is compared with SOTA SSL methods as well as fully supervised learning methods, which both cover CNN and transformer architectures.

Self-supervised methods: We compare HybridMIM with Models Genesis [10] and TransVW [14], which are the most recent multi-task SSL methods for 3D medical imaging. We also examine a masked image modeling-based SSL method, UNetFormer [15], which is built upon the SwinTransformer architecture. As ModelGenesis and TransVW officially release their pre-trained model weights, we skip the pre-training step and conduct finetuning on the four downstream segmentation tasks. For UNetFormer, we use its public codes and experiment with it in both evaluation modes.

Supervised methods: We also make comparison with state-of-the-art supervised segmentation methods in medical imaging. SegresNet [33] is a CNN-based architecture with good performance. UNETR [34] and SwinUNETR [25] are the most recent transformer-based methods for 3D medical image segmentation, which use vision transformer and SwinTransformer structures as encoders, respectively. Here, we use their public codes in the experiments.

V. RESULTS

This section demonstrates the significance of our proposed HybridMIM method. First, we make comparison with the current state-of-the-art approaches from four aspects: downstream segmentation performance (quantitative and qualitative), annotation cost reduction, and pre-training speed. We then conduct ablation experiments to explain how to determine the optimal architectural parameters, and illustrate the contribution of each component to the performance of HybridMIM.

A. Quantitative Comparison to Previous Methods

BTCV multi-organ segmentation. The multi-organ segmentation results are listed in Table I, in which the first, second, and third best dice scores are marked in red, blue, and green colors, respectively. Among the comparative methods, we can see that those with self-supervised pre-training generally achieve averagely better results than those fully supervised methods. TransVW obtains the best average Dice of 82.27%, while for UNetFormer, its generic pre-trained model presents an average Dice of 82.44%, outperforming the task-specific pre-trained model UNetFormer* by 0.26%.

In comparison, our methods on both UNet and SwinTransformer architectures outperform most SOTA methods, and the generic pre-trained models get better performance than their task-specific pre-trained counterparts. Specifically, the generic pre-trained model HybridMIM(UNet) presents the highest average Dice of 83.00%, which is 0.56% better than the best SOTA model UNetFormer, and outperforms it in 9 out of 13 segmentation targets. Furthermore, the task-specific pre-trained model HybridMIM*(Swin) segmented significantly better than the other methods on the Lag organ, reaching the Dice of 68.47%, which is 1.82% higher than the second place UNETR, while HybridMIM*(UNet) reports a significantly better result on the Gall organ, reaching a Dice of 78.67%.

Liver and liver tumor segmentation. As shown in Table II, our task-specific pre-trained model HybridMIM*(UNet) achieves the best average Dice of 74.36%, with an improvement of 0.48% over the second-place TransVW method. Furthermore, it reports the best Dice of 96.35% for the segmentation of the liver, which is 0.68% better than the second place TransVW; and obtains a Dice of 52.38% in the segmentation of liver tumors, only slightly lower than the second place ModelGen method with 52.53%. For the HD95 segmentation metric, the HybridMIM*(UNet) gets an average HD95 of 10.28, ranked in the third place. In addition, compared to the SwinUNETR method without pre-training, both HybridMIM*(Swin) and HybridMIM(Swin) which employ SwinUNETR as the underlying architecture, have more significant improvements in all the metrics.

TABLE I: Quantitative comparison on BTCV multi-organ segmentation dataset. Note: Spl: spleen, RKid: right kidney, LKid: left kidney, Gall: gallbladder, Eso: esophagus, Liv: liver, Sto: stomach, Aor: aorta, IVC: inferior vena cava, PSV: portal and splenic veins, Pan: pancreas, Rag: right adrenal glands, Lag: left adrenal glands. The task-specific pre-trained models are marked with *.

Methods	Avg	Spl	RKid	LKid	Gall	Eso	Liv	Sto	Aor	IVC	PSV	Pan	Rag	Lag
Segresnet	81.29	94.55	93.35	93.41	75.59	73.44	95.96	80.89	89.00	84.24	71.48	79.12	65.51	60.07
UNETR	81.33	94.66	94.27	94.09	65.23	74.20	96.90	80.06	89.16	84.04	73.46	80.32	64.30	66.65
SwinUNETR	81.81	94.72	94.23	93.89	66.60	74.54	96.63	78.77	89.79	83.64	74.69	82.19	67.76	66.18
ModelGen	81.45	91.99	93.52	91.81	65.11	76.14	95.98	86.88	89.29	83.59	71.79	81.62	67.97	63.18
TransVW	82.27	95.56	94.20	94.59	70.42	73.25	96.51	85.65	90.44	85.80	73.19	81.91	66.17	61.62
UNetFormer*	82.18	94.27	94.15	93.80	75.86	75.05	96.72	81.74	90.13	83.32	72.41	79.90	67.06	63.95
UNetFormer	82.44	95.90	94.61	94.28	71.51	75.08	96.51	81.46	90.06	85.84	75.34	80.72	68.50	61.78
HybridMIM*(Swin)	82.41	95.95	94.60	94.36	65.79	75.46	96.74	82.54	90.14	84.80	74.02	80.36	67.87	68.47
HybridMIM*(UNet)	82.62	95.27	94.25	94.15	78.67	74.24	96.68	83.31	90.25	85.82	73.07	80.24	65.02	62.94
HybridMIM(Swin)	82.63	95.95	94.25	94.26	72.56	74.14	96.78	79.25	90.17	85.10	73.64	81.83	69.21	66.88
HybridMIM(UNet)	83.00	95.68	94.43	94.40	74.33	75.84	96.72	82.92	90.86	86.43	72.96	81.16	66.98	66.25

TABLE II: The MSD Liver dataset requires segmentation of the liver and the corresponding tumor. and the MSD Spleen dataset requires segmentation of the spleen.

Organ	Liver						Spleen	
	Dice liver	Dice tumor	Dice Avg	HD liver	HD tumor	HD Avg	Dice	HD
SegresNet	95.53	48.26	71.90	0.81	15.31	25.31	94.10	0.5
UNETR	93.07	33.59	63.33	1.26	30.50	15.88	94.04	0.58
SwinUNETR	95.14	45.11	70.13	0.89	21.31	11.11	94.61	0.25
ModelGen	95.22	52.53	73.87	0.67	18.83	9.75	94.43	0.63
TransVW	95.67	52.10	73.88	0.60	21.36	10.98	95.55	0.41
UNetFormer*	95.50	49.81	72.65	0.52	21.72	11.12	95.36	0.25
UNetFormer	95.83	50.25	73.04	0.43	18.66	9.55	95.59	0.30
HybridMIM*(Swin)	95.45	50.19	72.82	0.69	15.21	7.95	95.87	0.25
HybridMIM*(UNet)	96.35	52.38	74.36	0.59	19.98	10.28	95.94	0.20
HybridMIM(Swin)	95.86	50.45	73.16	0.42	17.36	8.89	95.97	0.20
HybridMIM(UNet)	95.70	52.81	74.26	0.27	18.25	9.26	96.05	0.20

Spleen segmentation. The spleen segmentation results are listed on the right side of Table II. The HybridMIM based on both UNet and SwinUNETR architectures presented improved performance, both on Dice and HD95. HybridMIM(UNet) obtains Dice and HD95 with 96.05 and 0.20, respectively, improving the Dice score by 0.50% compared to TransVW, and by 2.1% compared to UNETR. Among the fully supervised methods, SwinUNETR gets the best Dice score of 94.61, and HD 0.25. Our generic pre-trained model HybridMIM(Swin) further improves SwinUNETR to achieve a Dice score of 95.97, realizing an increase of 1.36%.

Brain tumor segmentation. The segmentation results of gliomas for BraTS2020 dataset are summarized in Table III. WT, TC, ET represent whole tumor region, tumor core, and enhanced tumor region, respectively, and Avg is the Dice mean of the three segmentation targets. Our task-specific pre-trained model HybridMIM*(Swin) reports the best in WT, ET, and Avg with 91.48%, 80.81%, and 86.39% respectively. As for UNet as the underlying architecture, the generic pre-trained model HybridMIM(UNet) achieves Dice scores of 90.41%, 86.49%, and 80.61% for the three segmentation targets, respectively. Compared with ModelGen which is also built on UNet, we has the average Dice improved by 0.12%. It is also noted that on BraTS2020 dataset, the task-specific pre-trained mode

TABLE III: Quantitative comparison on BraTS 2020 dataset, which contains four modalities and three segmentation targets.

Methods	WT	TC	ET	Avg
SegresNet	90.04	85.08	78.81	84.64
UNETR	89.92	84.79	79.51	84.74
SwinUNETR	90.08	85.19	80.01	85.09
ModelGen	90.60	86.59	79.95	85.71
TransVW	90.96	86.26	80.20	85.80
UNetFormer*	90.93	86.17	79.97	85.69
UNetFormer	90.71	86.22	80.19	85.71
HybridMIM*(Swin)	91.48	86.88	80.81	86.39
HybridMIM*(UNet)	90.62	86.28	80.17	85.69
HybridMIM(Swin)	90.95	87.34	80.71	86.33
HybridMIM(UNet)	90.41	86.49	80.61	85.83

gets better performance than the generic pre-trained mode.

B. Qualitative Comparison to Previous Methods

To compare the segmentation results of different methods more intuitively, we choose HybridMIM(Swin) and four comparative methods with better performance on the BraTS2020, Liver, and BTCV datasets for visual comparison. As shown in Figure 3, HybridMIM(Swin) can improve the accuracy and completeness of lesion identification, and still perceive subtle lesions. To be specific, for brain tumor in BraTS2020 (the first row of Figure 3), our method segments the whole tumor with more accurate boundary, while the comparative methods all enlarge the tumor region. In the liver segmentation task (the second row), we can clear see that the comparative methods generate obvious discontinuity in the segmented areas. Especially UNETR and SegResNet fail to detect the lower part of the liver, while the detected liver region from our method exhibits a clearly higher integrity. For the BTCV dataset, TransVW, UNetFormer, SwinUNETR generates small holes in stomach; ModelGen even is subjected to a much large missing detected part. In contrast, our segmentation result is more close to the ground truth.

C. Reduce Manual Labeling Efforts

To evaluate the transfer learning ability with annotation scarcity challenge in medical imaging, we conduct the experiment of finetuning using a subset of BraTS2020 data.

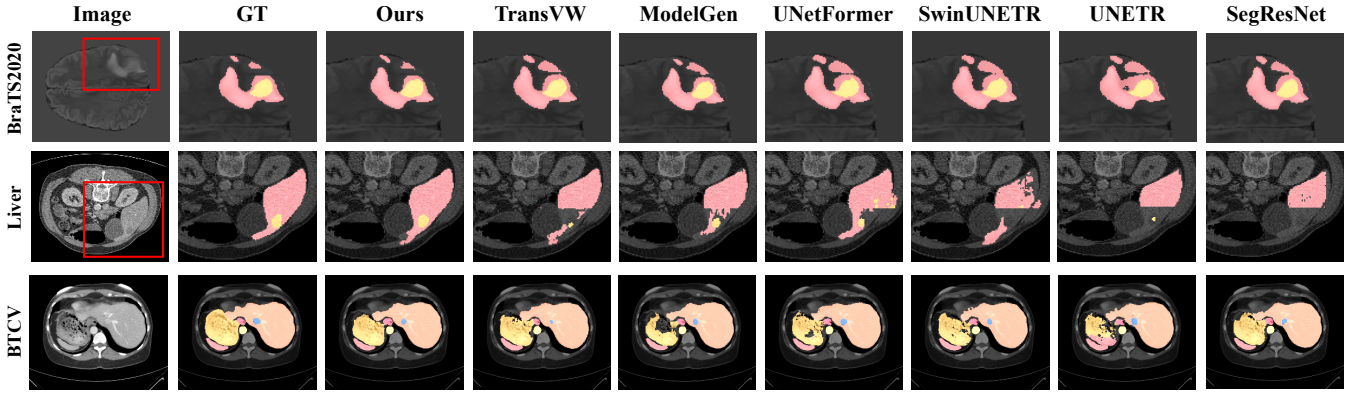


Fig. 3: Qualitative visualizations of the proposed HybridMIM and baseline methods. “Ours” is the HybridMIM(Swin) method. The three rows of visual comparison results are from BraTS2020, Liver, and BTCV datasets. Our proposed method is better for segmenting tiny lesions (first row) and has higher segmentation integrity (second row, third row).

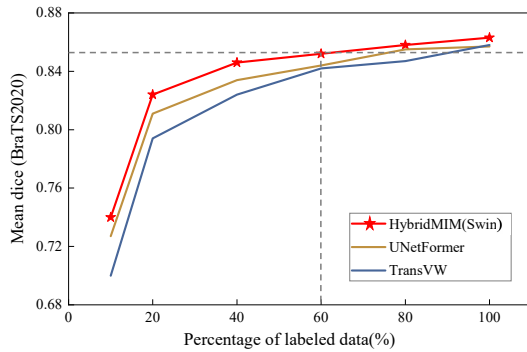


Fig. 4: Effect of different labeled data sizes on migration learning results. We selected 10%, 20%, 40%, 60%, 80%, and 100% of the training data in the BraTS2020 dataset to verify the transfer learning ability in different self-supervised learning methods.

Figure 4 demonstrates the comparison results between HybridMIM(Swin), TransVW and UNetFormer. It is clear that the generic pre-trained model HybridMIM(Swin) presents the best performance when using the same portion of labeled data. On employing 20% labelled data, HybridMIM(Swin) already achieves an average Dice of 82.55%, with 1.42% and 3.17% higher than UNetFormer and TransVW, respectively. The Dice 85.24% can be achieved by using HybridMIM(Swin) with 60% labelled data, while UNetFormer requires about 80% data and TransVW requires nearly 90% data.

D. Pre-training Speed Comparison

In self-supervised learning, the training speed is a notable factor to consider, because the unlabeled data scale is usually large especially in the generic training mode. Figure 5 demonstrates the time consumption of those self-supervised methods in the pre-training stage on BraTS2020 dataset. For a fair comparison, we count the average time of running one step for each method, which contains forward prediction, backward propagation, and updating network parameters, but does not include data reading and preprocessing operations.

As Figure 5 shows, the TransVW and ModelGenesis methods with the same underlying architecture have the highest time consumption, both of which are 1.42s per step. HybridMIM(Swin), when predicting all the masked sub-volumes

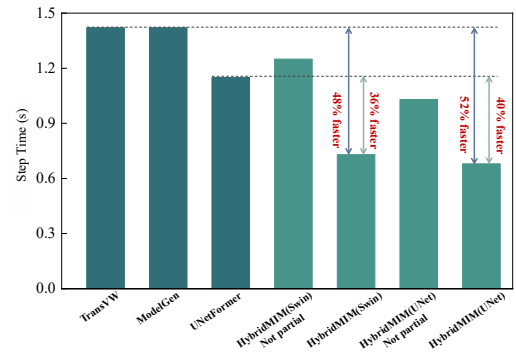


Fig. 5: Comparison of pre-training time consumption for different SSL methods. “Not partial” denotes that the partial region prediction scheme is not used.

(denoted as “Not partial”; see the fourth bar), has a higher time consumption than the UNetFormer method. It is because that although they have the similar underlying architecture, HybridMIM(Swin) involves more loss functions. On the other hand, when we apply the partial region prediction, the pre-training time of HybridMIM(Swin) decreases dramatically, in which the speedup is 48% with respect to TransVW and ModelGen, and 36% against UNetFormer.

When using the HybridMIM(UNet) method, there is a lower time consumption due to the structural simplicity of the UNet (see the rightmost two bars). The partial region prediction enables it to get a significant improvement in the pre-training speed, with the time consumption per step reduced by 0.35s. HybridMIM(UNet) achieves a pre-training speed of 0.68s, 52% faster than the TransVW and ModelsGenesis methods, and 40% faster than the UNetFormer method.

E. Ablation Study

1) *Selection of the optimal architecture settings:* In order to choose an optimal architecture setting, we conduct a multi-group control experiment. We choose the UNet architecture to pre-train the possible settings (see Figure 6), where the three numbers under each bar represent the first-level sub-volume size, the second-level patch size, and the region size for partial region prediction. The left vertical coordinates are the Dice metrics of finetuning the generic pre-trained model

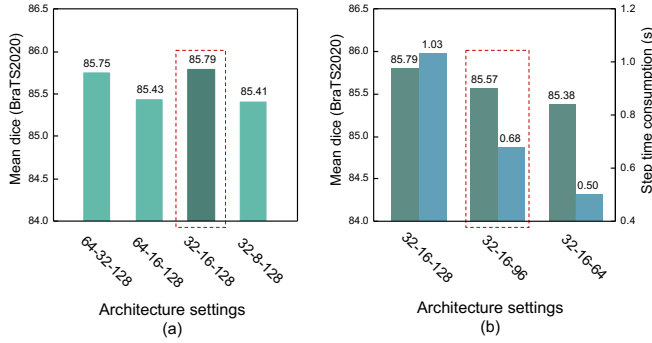


Fig. 6: Effect of different architecture parameters on transfer learning performance and pre-training time. The a-b-c in the horizontal coordinates in (a) represent the first-level, second-level, and reconstructed region sizes, respectively. The vertical coordinates represent the transfer learning capability in the BraTS2020 dataset (average Dice for the three segmentation targets). The right vertical coordinate in (b) indicates the time consumed per step during pre-training. The two red dashed boxes indicate the optimal architectural parameters we choose in (a) and (b), respectively.

on the BraTS2020 dataset. The right vertical coordinate in Figure 6 (b) is the time consumption of each pre-training step.

As Figure 6 (a) shows, we first fix the region size for partial region prediction to be 128, select four sets of parameters (64-32, 64-16, 32-16, and 32-8) for sub-volume and patch sizes. The results show that the parameter setting of 32-16-128 performs the best and achieves the best Dice of 85.79%.

Afterwards, we fix the optimal sub-volume and patch sizes (32-16), and gradually decrease the reconstruction region size; see Figure 6 (b). We can see that with a smaller reconstruction region size, the Dice score decreases a little bit, while the time performance reduces greatly. For instance, when reducing the reconstruction size from 128 to 96, the Dice score for the downstream segmentation task decreases from 85.79% to 85.57%, and the time per step decreases from 1.03s to 0.68s. Considering the trade-off between the segmentation accuracy and pre-training speed, we choose 32-16-96 as our architecture parameters for the case that the input sample has a size of $128 \times 128 \times 128$ (BraTS2020 dataset). Taking this experiments as guidance, we use an architectural parameter setting of 32-16-64 for the case that the input sample has a size of 96×96 (BTCV, MSD Liver and MSD Spleen).

2) Efficiency of Self-Supervised Objectives: We comprehensively validate the effectiveness of our modules through ablation experiments on the BraTS2020 dataset. The experimental results using the generic pre-training mode are presented in Table IV. We have five loss functions, namely \mathcal{L}_{PR} (partial region prediction), \mathcal{L}_{Num} (number prediction), \mathcal{L}_{Loc} (location prediction), \mathcal{L}_{Con} (consistency between number and location prediction), and \mathcal{L}_{CL} (contrastive learning). \mathcal{L}_{PR} facilitates the learning of 3D medical image latent representations at the pixel level; the combination of \mathcal{L}_{Num} , \mathcal{L}_{Loc} , and \mathcal{L}_{Con} facilitates the learning at the region level; and \mathcal{L}_{CL} facilitates the learning at the sample level. We make comparison to the baseline with supervised training from scratch on the BraTS2020 dataset (see the first row for each backbone).

UNet architecture. The baseline that is trained from scratch reports the Dice scores 89.75%, 84.65%, and 78.83%, for the three segmentation targets respectively, with an average num-

TABLE IV: Ablation experiments are performed on the BraTS2020 dataset. \mathcal{L}_{LR} : the local reconstruction loss, \mathcal{L}_{Num} : the number distribution prediction loss, \mathcal{L}_{Loc} : the location distribution prediction loss, \mathcal{L}_{Con} : the consistency loss, \mathcal{L}_{CL} : the contrastive learning loss.

Backbone	Loss	Segmentation Target			
		WT	TC	ET	Avg
UNet	Supervised learning	89.75	84.65	78.83	84.41
	\mathcal{L}_{PR}	90.19	85.50	79.48	85.06
	$\mathcal{L}_{PR} + \mathcal{L}_{Num}$	90.05	85.48	79.97	85.17
	$\mathcal{L}_{PR} + \mathcal{L}_{Num} + \mathcal{L}_{Loc}$	90.15	85.65	80.10	85.30
	$\mathcal{L}_{PR} + \mathcal{L}_{Num} + \mathcal{L}_{Loc} + \mathcal{L}_{Con}$	90.30	85.36	80.56	85.40
	$\mathcal{L}_{PR} + \mathcal{L}_{Num} + \mathcal{L}_{Loc} + \mathcal{L}_{Con} + \mathcal{L}_{CL}$	90.62	86.28	80.17	85.69
Swin	Supervised learning	90.08	85.19	80.01	85.09
	\mathcal{L}_{PR}	90.95	86.17	80.22	85.78
	$\mathcal{L}_{PR} + \mathcal{L}_{Num}$	90.93	86.94	80.48	86.12
	$\mathcal{L}_{PR} + \mathcal{L}_{Num} + \mathcal{L}_{Loc}$	91.18	86.33	81.10	86.20
	$\mathcal{L}_{PR} + \mathcal{L}_{Num} + \mathcal{L}_{Loc} + \mathcal{L}_{Con}$	90.98	87.06	80.71	86.24
	$\mathcal{L}_{PR} + \mathcal{L}_{Num} + \mathcal{L}_{Loc} + \mathcal{L}_{Con} + \mathcal{L}_{CL}$	91.48	86.88	80.81	86.39

ber of 84.41%. At this point, we add the first self-supervised learning loss \mathcal{L}_{PR} , which reconstructs the masked regions of the original image at the pixel level. The model weights finetuned onto the downstream segmentation task, result in a Dice average of 85.06%, with an improvement of 0.65% over the baseline. The addition of region-perception losses, i.e. \mathcal{L}_{Num} , \mathcal{L}_{Loc} , \mathcal{L}_{Con} , improves the model's ability to characterize the distribution of spatial regions, and the mean Dice value is increased from 85.06% to 85.40%, getting an improvement of 0.34%. Finally, we add the sample-level self-supervised loss \mathcal{L}_{CL} to enhance the model's ability to distinguish between different sample representations. With \mathcal{L}_{CL} , the mean Dice score reaches 85.69% in the downstream segmentation task, and the highest Dice scores of 90.62% and 86.28% on WT and TC, respectively. In the end, the average Dice score with pre-training was 1.29% higher than that without pre-training.

SwinUNETR architecture. Similarly, the HybridMIM method also achieves obvious improvements for the SwinUNETR architecture. The average Dice score of the three segmentation targets was finally improved from 85.09% without pre-training to 86.39%, achieving SOTA segmentation results on the BraTS2020 dataset.

Analysis of self-supervised loss enhancement effects. For the UNet and SwinTransformer architectures, Table IV shows that the \mathcal{L}_{PR} plays a larger role. The average Dice score of the three segmentation targets increases by 0.65% with the aid of \mathcal{L}_{PR} upon the UNet architecture, while the average Dice score of the three metrics increased by 0.69% upon the SwinTransformer architecture. The region perception losses (\mathcal{L}_{Num} , \mathcal{L}_{Loc} , \mathcal{L}_{Con} together) are the second important. Also note that although the \mathcal{L}_{Con} has a relatively small improvement for the downstream segmentation task, it has a role in keeping the predicted quantity consistent with the location information, improving the interpretability of the self-supervised learning.

VI. CONCLUSION

In this paper, we propose a Hybrid Masked Image Modeling framework for 3D medical image segmentation pre-training, which can support CNN and Transformer structures. The core of HybridMIM is a multi-level SSL strategy that learns anatomical features of 3D medical images from the pixel-level, region-level, and sample-level, respectively. Compared with other SSL methods, HybridMIM learns spatial anatomical

features of medical image data more effectively through a hierarchical masking approach, which supports pixel-level partial region prediction and region-level patch-masking perception. In addition, HybridMIM uses dropout-based contrastive learning at the sample level to enhance the model's ability to discriminate between different data.

We conduct a thorough comparison with both state-of-the-art SSL methods and supervised learning using segmentation datasets of multiple organs. The experimental results show that after pre-training by HybridMIM, the original network can get outperformed segmentation results. We also demonstrate the effectiveness of each loss function in HybridMIM on the UNet architecture and SwinUNETR architecture through comprehensive ablation experiments, and demonstrate the pre-training speed advantage of the proposed HybridMIM. In the future, we will apply HybridMIM pre-training on more architectures to support other downstream tasks.

REFERENCES

- [1] G. Litjens, T. Kooi, B. E. Bejnordi, A. A. A. Setio, F. Ciompi, M. Ghafoorian, J. A. Van Der Laak, B. Van Ginneken, and C. I. Sánchez, "A survey on deep learning in medical image analysis," *Medical image analysis*, vol. 42, pp. 60–88, 2017.
- [2] M. W. Khan, "A survey: Image segmentation techniques," *International Journal of Future Computer and Communication*, vol. 3, no. 2, p. 89, 2014.
- [3] F. Shamsad, S. Khan, S. Zamir, M. Khan, M. Hayat, F. Khan, and H. Fu, "Transformers in medical imaging: A survey. arxiv 2022," *arXiv preprint arXiv:2201.09873*.
- [4] N. Tajbakhsh, L. Jeyaseelan, Q. Li, J. N. Chiang, Z. Wu, and X. Ding, "Embracing imperfect datasets: A review of deep learning solutions for medical image segmentation," *Medical Image Analysis*, vol. 63, p. 101693, 2020.
- [5] S. Atito, M. Awais, and J. Kittler, "Sit: Self-supervised vision transformer," *arXiv preprint arXiv:2104.03602*, 2021.
- [6] Z. Dai, B. Cai, Y. Lin, and J. Chen, "Up-detr: Unsupervised pre-training for object detection with transformers," in *Proceedings of the IEEE/CVF conference on computer vision and pattern recognition*, 2021, pp. 1601–1610.
- [7] J. Liang, J. Cao, G. Sun, K. Zhang, L. Van Gool, and R. Timofte, "Swinir: Image restoration using swin transformer," in *Proceedings of the IEEE/CVF International Conference on Computer Vision*, 2021, pp. 1833–1844.
- [8] C. Doersch and A. Zisserman, "Multi-task self-supervised visual learning," in *Proceedings of the IEEE international conference on computer vision*, 2017, pp. 2051–2060.
- [9] S. Gidaris, P. Singh, and N. Komodakis, "Unsupervised representation learning by predicting image rotations," *arXiv preprint arXiv:1803.07728*, 2018.
- [10] Z. Zhou, V. Sodha, J. Pang, M. B. Gotway, and J. Liang, "Models genesis," *Medical image analysis*, vol. 67, p. 101840, 2021.
- [11] T. Gao, X. Yao, and D. Chen, "Simcse: Simple contrastive learning of sentence embeddings," *arXiv preprint arXiv:2104.08821*, 2021.
- [12] K. He, X. Chen, S. Xie, Y. Li, P. Dollár, and R. Girshick, "Masked autoencoders are scalable vision learners," in *Proceedings of the IEEE/CVF Conference on Computer Vision and Pattern Recognition*, 2022, pp. 16 000–16 009.
- [13] Y. Tang, D. Yang, W. Li, H. R. Roth, B. Landman, D. Xu, V. Nath, and A. Hatamizadeh, "Self-supervised pre-training of swin transformers for 3d medical image analysis," in *Proceedings of the IEEE/CVF Conference on Computer Vision and Pattern Recognition*, 2022, pp. 20 730–20 740.
- [14] F. Haghghi, M. R. H. Taher, Z. Zhou, M. B. Gotway, and J. Liang, "Transferable visual words: Exploiting the semantics of anatomical patterns for self-supervised learning," *IEEE transactions on medical imaging*, vol. 40, no. 10, pp. 2857–2868, 2021.
- [15] L. Wang, R. Li, C. Zhang, S. Fang, C. Duan, X. Meng, and P. M. Atkinson, "Unetformer: A unet-like transformer for efficient semantic segmentation of remote sensing urban scene imagery," *ISPRS Journal of Photogrammetry and Remote Sensing*, vol. 190, pp. 196–214, 2022.
- [16] Z. Xie, Z. Zhang, Y. Cao, Y. Lin, J. Bao, Z. Yao, Q. Dai, and H. Hu, "Simmim: A simple framework for masked image modeling," in *Proceedings of the IEEE/CVF Conference on Computer Vision and Pattern Recognition*, 2022, pp. 9653–9663.
- [17] B. H. Menze, A. Jakab, S. Bauer, J. Kalpathy-Cramer, K. Farahani, J. Kirby, Y. Burren, N. Porz, J. Slotboom, R. Wiest *et al.*, "The multimodal brain tumor image segmentation benchmark (brats)," *IEEE transactions on medical imaging*, vol. 34, no. 10, pp. 1993–2024, 2014.
- [18] S. Bakas, H. Akbari, A. Sotiras, M. Bilello, M. Rozycki, J. S. Kirby, J. B. Freymann, K. Farahani, and C. Davatzikos, "Advancing the cancer genome atlas glioma mri collections with expert segmentation labels and radiomic features," *Scientific data*, vol. 4, no. 1, pp. 1–13, 2017.
- [19] L. B. X. Z, I. J. S. M, L. T, and K. A, "Miccai multi-atlas labeling beyond the cranial vault– workshop and ch5allenge," 2015.
- [20] M. Antonelli, A. Reinke, S. Bakas, K. Farahani, A. Kopp-Schneider, B. A. Landman, G. Litjens, B. Menze, O. Ronneberger, R. M. Summers *et al.*, "The medical segmentation decathlon," *Nature communications*, vol. 13, no. 1, pp. 1–13, 2022.
- [21] D. Pathak, P. Krahenbuhl, J. Donahue, T. Darrell, and A. A. Efros, "Context encoders: Feature learning by inpainting," in *Proceedings of the IEEE conference on computer vision and pattern recognition*, 2016, pp. 2536–2544.
- [22] M. Noroozi and P. Favaro, "Unsupervised learning of visual representations by solving jigsaw puzzles," in *Computer Vision–ECCV 2016: 14th European Conference, Amsterdam, The Netherlands, October 11–14, 2016, Proceedings, Part VI*. Springer, 2016, pp. 69–84.
- [23] L. Chen, P. Bentley, K. Mori, K. Misawa, M. Fujiwara, and D. Rueckert, "Self-supervised learning for medical image analysis using image context restoration," *Medical image analysis*, vol. 58, p. 101539, 2019.
- [24] O. Ronneberger, P. Fischer, and T. Brox, "U-net: Convolutional networks for biomedical image segmentation," in *International Conference on Medical Image Computing and Computer-Assisted Intervention*. Springer, 2015, pp. 234–241.
- [25] A. Hatamizadeh, V. Nath, Y. Tang, D. Yang, H. R. Roth, and D. Xu, "Swin unetr: Swin transformers for semantic segmentation of brain tumors in mri images," in *International MICCAI Brainlesion Workshop*. Springer, 2022, pp. 272–284.
- [26] Z. Han, F. Yang, J. Huang, C. Zhang, and J. Yao, "Multimodal dynamics: Dynamical fusion for trustworthy multimodal classification," in *Proceedings of the IEEE/CVF Conference on Computer Vision and Pattern Recognition*, 2022, pp. 20 707–20 717.
- [27] M. Zhang, Y. Wu, H. Zhang, Y. Qin, H. Zheng, J. Sun, G.-Z. Yang, and Y. Gu, "Multi-site, multi-domain airway tree modeling (atm'22)," 2022.
- [28] A. A. A. Setio, A. Traverso, T. De Bel, M. S. Berens, C. Van Den Bogaard, P. Cerello, H. Chen, Q. Dou, M. E. Fantacci, B. Geurts *et al.*, "Validation, comparison, and combination of algorithms for automatic detection of pulmonary nodules in computed tomography images: the luna16 challenge," *Medical image analysis*, vol. 42, pp. 1–13, 2017.
- [29] H. R. Roth, Z. Xu, C. Tor-Diez, R. S. Jacob, J. Zember, J. Molto, W. Li, S. Xu, B. Turkbey, E. Turkbey *et al.*, "Rapid artificial intelligence solutions in a pandemic—the covid-19-20 lung ct lesion segmentation challenge," *Medical image analysis*, vol. 82, p. 102605, 2022.
- [30] J. Ma, Y. Zhang, S. Gu, X. An, Z. Wang, C. Ge, C. Wang, F. Zhang, Y. Wang, Y. Xu, S. Gou, F. Thaler, C. Payer, D. Štern, E. G. Henderson, D. M. McSweeney, A. Green, P. Jackson, L. McIntosh, Q.-C. Nguyen, A. Qayyum, P.-H. Conze, Z. Huang, Z. Zhou, D.-P. Fan, H. Xiong, G. Dong, Q. Zhu, J. He, and X. Yang, "Fast and low-gpu-memory abdomen ct organ segmentation: The flare challenge," *Medical Image Analysis*, vol. 82, p. 102616, 2022.
- [31] I. Loshchilov and F. Hutter, "Decoupled weight decay regularization," *arXiv preprint arXiv:1711.05101*, 2017.
- [32] K. He, X. Zhang, S. Ren, and J. Sun, "Deep residual learning for image recognition," in *Proceedings of the IEEE conference on computer vision and pattern recognition*, 2016, pp. 770–778.
- [33] A. Myronenko, "3d mri brain tumor segmentation using autoencoder regularization," in *International MICCAI Brainlesion Workshop*. Springer, 2018, pp. 311–320.
- [34] A. Hatamizadeh, Y. Tang, V. Nath, D. Yang, A. Myronenko, B. Landman, H. R. Roth, and D. Xu, "Unetr: Transformers for 3d medical image segmentation," in *Proceedings of the IEEE/CVF Winter Conference on Applications of Computer Vision*, 2022, pp. 574–584.